IEEE Access
Multidisciplinary | Rapid Review | Open Access Journal

Received June 5, 2018, accepted July 16, 2018, date of publication July 25, 2018, date of current version August 20, 2018.

Digital Object Identifier 10.1109/ACCESS.2018.2859786

Automatic Coronary Centerline Extraction Using Gradient Vector Flow Field and Fast Marching Method From CT Images

HENGFEI CUI AND YONG XIA

Shaanxi Provincial Key Laboratory of Speech and Image Information Processing, School of Computer Science and Engineering, Northwestern Polytechnical University, Xi'an 710072, China

Centre for Multidisciplinary Convergence Computing, School of Computer Science and Engineering, Northwestern Polytechnical University, Xi'an 710072, China

Corresponding author: Hengfei Cui (hfcui@nwpu.edu.cn)

This work was supported in part by the China Postdoctoral Science Foundation under Grant 2017M623245, in part by the National Natural Science Foundation of China under Grant 61471297 and Grant 61771397, and in part by the Fundamental Research Funds for the Central Universities under Grant 3102018zy031.

ABSTRACT In current medical imaging, coronary artery stenosis quantification requires fast and accurate coronary centerline computation. This paper develops a new framework for extracting coronary centerlines from 3-D segmented coronary arteries models. The approach utilizes the gradient vector flow (GVF) filed-based speed image of the vessel model and implements a wavefront propagation technique for centerline branch tracking. The approach was validated over 17 3-D synthetic vessel models. The results showed a good agreement between the proposed method and ground truth centerline in synthetic vessel models with an average distance of 0.25 mm and overlap measure of 96.0%, given the CT scans with a resolution of about 0.3 mm $\times$ 0.3mm $\times$ 0.4mm. Second, the proposed method was further tested in six clinical coronary arteries models reconstructed from computed tomography coronary angiography in human patients and found to be applicable in both left coronary arteries and right coronary arteries with an average processing time of 16 minutes per case. In conclusion, the proposed GVF field and the fast marching-based method should have more routine clinical applicability.

INDEX TERMS Computed tomography angiography, coronary centerline, fast marching method, gradient vector flow, vessel segmentation.

I. INTRODUCTION

Coronary centerline computation plays an utmost role in cardiovascular disease screening [1]–[3], since it holds great significance for coronary artery stenosis quantification and provides important pathological information. However, the performance of centerline tracking technique varies easily due to noises and artifacts. Moreover, it is a grand challenge to identify the vascular directions at intersections or overlapping. Furthermore, manual extraction and annotation is skill-demanding and time-consuming. Therefore, accurate algorithms for coronary centerline tracking with minimal user interaction are in demand.

At present, several approaches are dedicated to coronary centerline extraction, such as mathematical morphology [4], medialness filter [5] and fuzzy connectedness [6]. An overview of available centerline extraction techniques are presented in [7]. Topology- or connectivity-preserving thinning is usually used for computing centerlines [8]. In [9], a smoothing approach is introduced for lung airways, which is based on an ellipsoidal kernel before segmenting and thinning the 3D volumetric image. Bullitt *et al.* [10] developed a ridge line detection method to identify centerlines, which uses the Hessian of the image intensity. Aylward and Bullitt [11] introduced a method based on intensity ridge traversal. The resulting centerlines are smoothed using a B-spline-based approach. The approach by Zhang *et al.* [12] is based on Dijkstras algorithm using a distance field cost function. Besides, the extraction algorithm described by Wischgoll *et al.* [13] is based on a topological analysis of a vector field generated by normal vectors of the extracted vessel wall. Zheng *et al.* [14] developed a new mean centerline generation method by combining model-driven and data-driven approaches.

Due to the existence of narrowing and calcification, these methods can not compute distal parts of coronary centerlines accurately. In addition, all the methods are designed for their own purpose and detection ability, thus their performances vary according to the values of their parameters and thresholds. Moreover, many existing algorithms do not consider the shape of each vessel, which may provide important information for clinical diagnosis.

In the present context, numerous algorithms for centerline extraction have been developed based on various medial functions [15]–[17]. For example, some approaches depend on the concept of distance filed. At each voxel location, the distance field computes the nearest distance from the vessel's boundary. In [15], the distance transform is calculated as a speed image, and the fast marching (FM) method is performed for centerline extraction. In [16], a modified distance field based speed image is proposed, which integrates the magnitude of Gaussian gradient. Therefore, further smoothing and pruning operations are usually required to obtain smooth centerline, especially in 3D case.

To overcome the aforementioned shortcomings, Hassouna and Farag [18] combined level set method and wave propagation technique. However, the parameters are heuristically selected, which prevents the algorithm from automation. Besides, the method is inefficient for large datasets since the processing time for distance map calculation is huge.

This paper develops a fast and accurate centerline extraction algorithm. The new algorithm can be described in two main parts: 1) Given the vessel segmentation results, the algorithm computes an initial medial function (speed image) based on gradient vector flow. 2) The algorithm automatically decides a source point and drive a wave using the GVF based speed image, computes a time arriving map and tracks the centerline branch along the gradient decent of the time arriving map. The first major contribution is to propose an enhanced Frangi's filter that can better detect the vesselness measures. More specifically, a novel vesselness diffusion filter is developed to enhance the intensities of the main branches. The second contribution is to use the GVF based medial function as the new speed image, which can guarantee the efficiency and accuracy. Thirdly, the multiple branch extraction algorithm uses the previously computed centerlines as the source points and drives new wave front propagations. Also high order Runge-Kutta method is applied to solve the discrete centerline extraction formulation.

A preliminary version of this work was presented in [19]. In this manuscript, we make extensions in the following aspects: 1) A more detailed description of the multiple centerline extraction procedure is given. 2) The theoretical support of 3D gradient vector flow is presented. Besides, superiority of the gradient of GVF over its magnitude is described. 3) We further provide comparison of processing time and overlap measure with Hassouna's improved GVF in [18]. 4) Our manuscript includes detailed studies of algorithm design, speed image construction, as well as numerical solution for single branch tracking. Fig. 1 shows the flowchart of the presented framework.

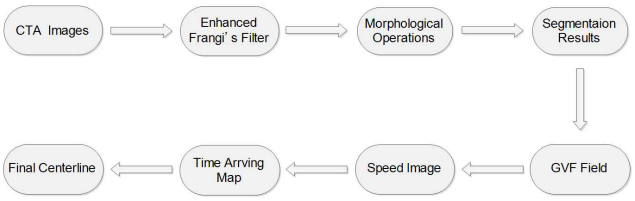

FIGURE 1. The pipeline of the centerline computation framework.

II. METHODOLOGIES

A. CORONARY ARTERY SEGMENTATION

The connected components based approach [20] is used to segment the entire coronary artery tree from CTCA dataset. Frangi's vesselness function [21] is formulated as:

$$\mathcal{V}_F(\vec{\lambda}) = \begin{cases} 0 & \text{if } \lambda_2 > 0 \text{ or } \lambda_3 > 0 \\ (1 - e^{-\frac{A^2}{2\alpha^2}}) \cdot e^{-\frac{B^2}{2\beta^2}} \cdot (1 - e^{-\frac{S^2}{2\gamma^2}}) & \text{otherwise} \end{cases} \tag{1}$$

where $|\lambda_1| \leq |\lambda_2| \leq |\lambda_3|$ are the eigenvalues of the Hessian, A, B and S are defined as follows to capture different vessel structures

$$A = \frac{|\lambda_2|}{|\lambda_3|} \tag{2}$$

$$B = \frac{|\lambda_1|}{\sqrt{|\lambda_2 \lambda_3|}} \tag{3}$$

$$S = \sqrt{\lambda_1^2 + \lambda_2^2 + \lambda_3^2} \tag{4}$$

and α, β and γ are weighting parameters. Although Frangi's filter is relatively efficient, it is sensitive to image noise. Meanwhile according to (1), small-scale vessels will be considered as artifacts easily since the enhancement effect is lower. Therefore, a multi-scale approach can be used to enhance tubular structures and reduce background noises, by performing vesselness diffusion.

Original CT images are usually evolved by applying the diffusion equation, whose divergence form can be expressed as:

$$L_t = \nabla \cdot (D \nabla L) \tag{5}$$

where L is the original image and D is the diffusion tensor. Unfortunately, $\mathcal{V}_F$ defined in (1) can not directly be used in (5) since it is not smooth at the origin. The enhanced vesselness function $\mathcal{V}_s$ is therefore proposed

$$\mathcal{V}_s(\sigma) = \begin{cases} 0 & \text{if } \lambda_2 \geq 0 \text{ or } \lambda_3 \geq 0 \\ e^{-\left(\frac{2c^2}{|\lambda_2|\lambda_3^2}\right)} (1 - e^{-\frac{A^2}{2\alpha^2}}) \cdot e^{-\frac{B^2}{2\beta^2}} \cdot (1 - e^{-\frac{S^2}{2\gamma^2}}) & \\ \text{otherwise} & \end{cases} \tag{6}$$

where the first term approaches zero near the origin and is one everywhere else. The multiscale approach can be performed, and the maximum vesselness response is selected as

$$\mathcal{V} = \max_{\sigma_{min} \leq \sigma \leq \sigma_{max}} \mathcal{V}_s(\sigma) \tag{7}$$

Intuitively, diffusion in the vessel direction should be steered and diffusion perpendicular to the vessel should be inhibited. Therefore, the novel diffusion tensor D incorporates the vesselness measure $\mathcal{V}$, and is given by [22] and [23]:

$$D \triangleq Q\Lambda' Q^T \tag{8}$$

where Q is the eigenvectors of $\mathcal{H}$. Moreover, three diagonal entries of the diagonal matrix Λ' are defined as:

$$\lambda_1' \triangleq 1 + (\omega - 1) \cdot \mathcal{V}^{\frac{1}{S}} \tag{9}$$

$$\lambda_2' \triangleq 1 + (\epsilon - 1) \cdot \mathcal{V}^{\frac{1}{S}} \tag{10}$$

$$\lambda_3' \triangleq 1 + (\epsilon - 1) \cdot \mathcal{V}^{\frac{1}{S}} \tag{11}$$

with parameters $S \in \mathbb{R}^+$, $\omega > \epsilon$ and $\epsilon > 0$. The diffusion strength parameter ω is normally larger than one. Besides, ϵ should be chosen as a small positive value to ensure the tensor's positive definiteness. The diffusion strength is maximal (ω) for tubular structures ($\mathcal{V} \to 1$). While for non-vessel structures ($\mathcal{V} \to 0$), the diffusion is isotropic and high. Finally, the parameter S will not alter the smoothness property. Fig. 2 shows a comparison of Frangi's vesselness, enhanced vesselness and the diffusion result. The main branch is enhanced and the background non-vessel structures are suppressed.

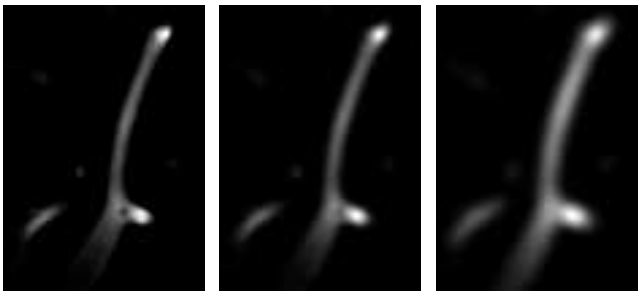

(a) (b) (c)

FIGURE 2. A comparison of Frangi's vesselness, enhanced vesselness and the diffusion result after 4 iterations. (a) Frangi's vesselness. (b) Enhanced vesselness. (c) Diffusion.

B. EDGE MAP

The edge map [24] $f(x)$ of the original segmentation result I(x) is given by

$$f^{(1)}(x) = |\nabla I(x)| \tag{12}$$

or

$$f^{(2)}(x) = |\nabla[G_\sigma(x) * I(x)]| \tag{13}$$

where $x = (x, y, z)$ and $G_\sigma(x)$ is the 3D Gaussian function. Edge maps generally have some nice properties. The gradient of an edge map ∇f is approximated to zero in homogeneous regions. At the edge locations, the ∇f vectors have large magnitudes and point toward the edges.

C. GRADIENT VECTOR FLOW

The 3D GVF field $V(x) = [u(x), v(x), w(x)]$ minimizes the following energy functional [25]

$$E_{GVF}(V) = \iiint \mu(|\nabla u(x)|^2 + |\nabla v(x)|^2 + |\nabla w(x)|^2) + |\nabla f(x)|^2 |V(x) - \nabla f(x)|^2 dx \tag{14}$$

where μ is the smoothness regularization parameter.

Using the calculus of variations [26], the GVF field must satisfy

$$\mu \nabla^2 V(t) - (V - \nabla f)|\nabla f|^2 = 0 \tag{15}$$

where ∇^2 is the Laplacian operator and t is the time variable. The GVF field can thus be determined by solving

$$V_t = \mu \nabla^2 V(t) - (V - \nabla f)|\nabla f|^2 \tag{16}$$

where V_t is the partial derivative of V. Compared to the distance field, the GVF magnitude ($|V(x)|$) does not form medial surfaces since that the GVF value at each pixel is computed by diffusion process [27].

D. SPEED IMAGE

In the previous work [18], $|V(x)|$ is used to construct a weak medial function, and the following medial function is proposed:

$$\lambda(x) = 1.0 - \left(\frac{|V(x)| - \min(|V|)}{\max(|V|) - \min(|V|)} \right)^{\gamma}, \quad 0 < \gamma < 1 \tag{17}$$

with field strength parameter γ. It can be seen that the magnitude of the GVF was normalized and the parameter γ was introduced for the purpose of controlling the strength of the medial function $\lambda(x)$. The value of γ was empirically determined. However, this value was determined by using a slab, which deviates too much from tubular structures (coronary arteries). Moreover, the value of γ is data-dependent, which prevents the whole centerline extraction algorithm from automation and reproduction.

To reduce the effect of the strength parameter γ on the accuracy of the medial function, the properties of the magnitude of the gradient of GVF, $|\nabla V(x)|$, is utilized in this work to construct the initial medial function. We first compute the gradient of GVF field $\nabla V(x)$. The centerlines and the edge points can be discerned by checking $|\nabla V(x)|$. For the purpose of extracting centerlines only, the edges need to be further removed after separating the smooth area. Therefore, an edge indicator function [28] is defined

$$g(x) = \frac{1}{1 + f(x)} \tag{18}$$

with very small values at the strong edge locations and 1 in other places. The centerline strength function is thus given by

$$k(x) = g(x) * |\nabla V(x)| \tag{19}$$

then normalizing it to [0, 1],

$$\bar{k}(x) = \left(\frac{k(x) - \min(k)}{\max(k) - \min(k)} \right)^{\gamma} \tag{20}$$

where γ is the field strength in [0, 1]. Once $|\nabla V(x)|$ is computed and the edge indicator function $g(x)$ is introduced, the accuracy of the new medial function is less dependent on the parameter γ. It can be proved that any value in (0, 1) can be selected. Without loss of generality, γ is chosen as 1 in this work.

Therefore, a new speed image based on $\bar{k}(x)$ [18] for the fast marching method

$$F = \mathrm{e}^{\beta \bar{k}} \tag{21}$$

where β is a speed parameter defined as $\beta = 1/\tau$ and τ is the parameter. The proposed speed image F is computationally efficient since it is directly computed from the GVF and there is no extra computation required.

E. BRANCH TRACING

Based on the proposed centerline strength function $\bar{k}(x)$, the source point P_s is chosen as the point with maximal value in $\bar{k}(x)$:

$$P_s = \arg \max_x \bar{k}(x) \tag{22}$$

Then a wave front is propagated using the new speed image F from the source P_s. The resulting map T can be treated as a modified distance map from medial function $\bar{k}(x)$, using a non Euclidean metric that gives larger value in the center of the vessel.

Fig. 3(a) shows a 2D example of tubular structures, whose properties of high curvature and multiple branches are capable of representing the vascular structures. Fig. 3(b) gives the computed time arriving map T of the wave front starting from the source point P_s, given the proposed speed image F.

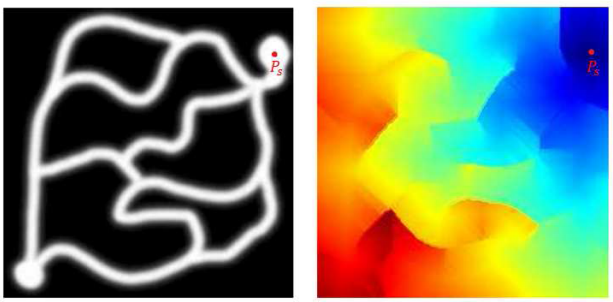

FIGURE 3. A 2D example of multiple vessel branches and the computed time arriving map of the wave front starting from the source point P_s.

Next the start point m_0 is chosen as the point with maximum T value, which is the furthest geodesic point. The first branch centerline is extracted by solving

$$\frac{dS}{dt} = -\frac{\nabla T}{|\nabla T|}, \quad S(0) = m_0 \tag{23}$$

where m_0 is the furthest geodesic point and $S(t)$ represents the discrete centerline. The classical implicit Runge-Kutta method [29] is explored, which is given as

$$S_{n+1} = S_n + \sum_{i=1}^{s} b_i k_i \tag{24}$$

where

$$k_i = hf\left(t_n + c_i h, S_n + \sum_{j=1}^{s} a_{ij} k_j\right) \tag{25}$$

here t_n is the time step and h is the step size.

The two-stage Gauss-Legendre method (order of 4) is applied to achieve higher accuracy. It can be shown that [30]:

$$k_1 = hf\left(t_n + (\frac{1}{2} - \frac{1}{6}\sqrt{3})h, S_n + \frac{1}{4}k_1 + (\frac{1}{4} - \frac{1}{6}\sqrt{3})k_2\right) \tag{26}$$

$$k_2 = hf\left(t_n + (\frac{1}{2} + \frac{1}{6}\sqrt{3})h, S_n + (\frac{1}{4} + \frac{1}{6}\sqrt{3})k_1 + \frac{1}{4}k_2\right) \tag{27}$$

Assume initial guesses of k_1 and k_2, denoted as k_1^0 and k_2^0, were linearly interpolated from the 8 nearest neighbours of m_0 in the gradient field ∇T and then used for the first branch tracking. To improve the efficiency, an iterative method [29] was used to solve this system of nonlinear equations. Once the first branch is determined, it will be used as the new wave front source points and all the remaining branches can be computed following the same tracking process. Fig. 4 illustrates a 2D example of multiple centerline branches formation. The whole procedure terminates when the length of the new branch is less than some pre-defined threshold value L. Algorithm 1 shows the pseudo-code of the whole procedure.

Algorithm 1 Centerline Computation Algorithm

Input: Segmentation result I
Output: Final centerline S_f
$S_f = \emptyset$, $linelength = \infty$
$P_s = \arg\max_x \bar{k}(x)$
$i = 0$
while $linelength > L$ **do**
  $T = FastMarching(P_s, F)$
  $m_i = x \mid T(x) \geq T(y)\ \forall x, y \in O$
  $S = backtrace(m_i, P_s)$
  $linelength = length(S)$
  $P_s = P_s + S$, $S_f = S_f + S$
  $i = i + 1$
end while

Note: $\bar{k}(x) = \left(\frac{k(x) - \min(k)}{\max(k) - \min(k)} \right)^{\gamma}$, $k(x) = g(x) * |\nabla V(x)|$ *and* $g(x) = \frac{1}{1+f(x)}$, *where* $V(x)$ *is GVF field,* $f(x)$ *is edge map,* γ *is the field strength in* [0, 1]. $F = \mathrm{e}^{\beta \bar{k}}$, *where* $\beta = 1/\tau$ *and* τ *is the parameter.*

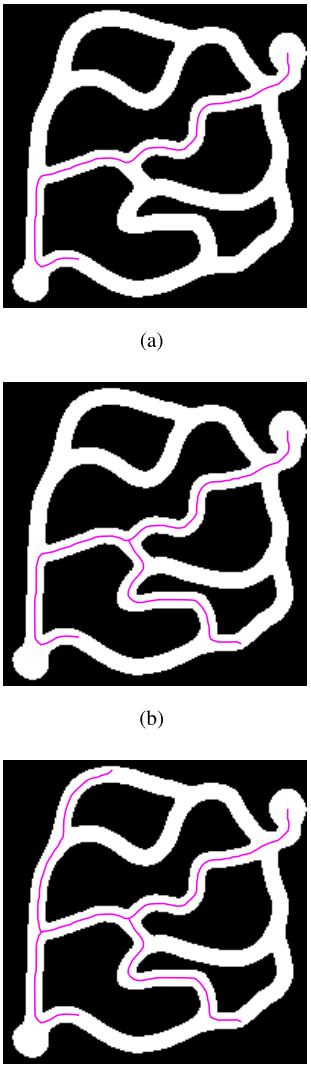

FIGURE 4. Multiple centerline branches formation.

III. RESULTS

A. VALIDATION

The testing datasets were provided by the MICCAI'08 workshop *3D Segmentation in the Clinic: A Grand Challenge II - Coronary Artery Tracking* [31]. A total of 8 patients were scanned, each of which has four different segments of coronary arteries extracted. In this work, a total of 17 segments of coronary artery models were reconstructed. Validation of the centerline extraction algorithm was performed using these 17 synthetic vessel models. Table 1 summarizes the dataset size and resolution of each CTCA dataset. All the experiments were implemented in Matlab 2014b on a Windows computer with 2.6 GHz CPU and 16 GB of RAM.

In the experiments, the edge maps were calculated according to Equation (13). The parameter $\mu = 0.2$ and iteration $n = 10$ were chosen for the GVF computation. The field strength parameter $\gamma = 1$ was used. Meanwhile, different values of γ between 0 and 1 were selected, which gave similar centerline results of the synthetic vessel model. This demonstrates one advantage of the proposed speed image. The step size for Runge-Kutta method is selected as 0.01.

TABLE 1. Dataset size and resolution of each CTA data.

	Size	Resolution (mm^3)
Dataset 1	512×512×272	0.3633×0.3633×0.4
Dataset 2	512×512×338	0.3633×0.3633×0.4
Dataset 3	512×512×288	0.334×0.334×0.4
Dataset 4	512×512×276	0.3711×0.3711×0.4
Dataset 5	512×512×274	0.3164×0.3164×0.4
Dataset 6	512×512×274	0.3223×0.3223×0.4
Dataset 7	512×512×268	0.3203×0.3203×0.4
Dataset 8	512×512×304	0.2871×0.2871×0.4

Fig. 5 demonstrates the computed edge maps of a 2D vessel cross section, for different values of parameter σ. Central pixel locations are observed to be discerned when σ is selected as 2. Fig. 6 shows a 2D example of gradient of the edge map and the gradient vector flow field, with $\sigma = 0.5$. In Fig. 7 we show the model Vessel 0, the ground truth centerline and result of applying the skeletonization algorithm. The computed centerline is observed to be continuous, naturally smooth and highly coincident with the ground truth centerline. The remaining 3D synthetic vessel models, together with the ground truth and the computed centerlines are presented in Fig. 8.

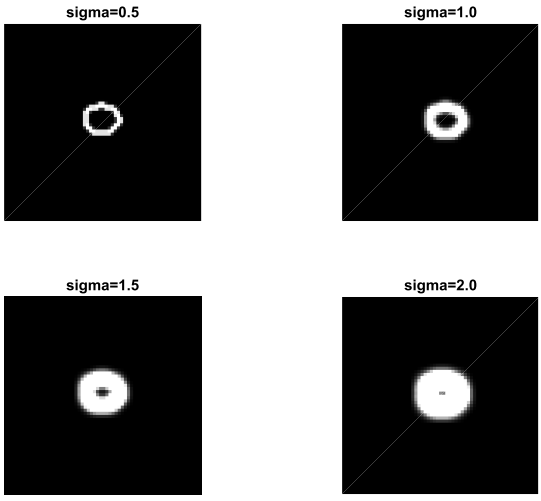

FIGURE 5. Edge maps for different values of parameter σ.

Moreover, a quantitative analysis was performed to explore the accuracy of the centerline extraction algorithm. The average error and maximum error in both world space and voxel space between the ground truth and computed centerlines for three different methods are presented in Table 2. For Van's method, the average distance and maximum distance in voxel space between the ground truth and computed centerlines were 0.65 ± 0.23 mm and 1.09 ± 0.37 mm, respectively. For DTFM method,

TABLE 2. A comparison of the average and maximum error for each of the synthetic vessel model between previous methods and the proposed method.

	Van's method [15]				DTFM method [16]				GVFFM method			
	L_2 norm		L_∞ norm		L_2 norm		L_∞ norm		L_2 norm		L_∞ norm	
	Voxel	World (mm)	Voxel	World (mm)	Voxel	World (mm)	Voxel	World (mm)	Voxel	World (mm)	Voxel	World (mm)
Vessel 0	2.29	0.88	3.02	1.20	2.26	0.85	3.00	1.11	**1.01**	**0.38**	**1.38**	**0.49**
Vessel 1	1.21	0.43	1.89	0.71	1.25	0.45	1.88	0.69	**0.49**	**0.18**	**0.98**	**0.29**
Vessel 2	2.86	1.06	5.05	1.92	**2.85**	**1.03**	**4.99**	**1.81**	2.92	1.07	5.01	1.90
Vessel 3	1.07	0.41	2.06	0.81	1.05	0.38	2.04	0.77	**0.37**	**0.13**	**0.93**	**0.29**
Vessel 4	1.66	0.65	2.52	0.95	1.65	0.63	2.51	0.93	**0.49**	**0.19**	**0.89**	**0.31**
Vessel 5	2.12	0.82	3.19	1.19	2.10	0.79	3.18	1.18	**0.77**	**0.32**	**1.24**	**0.43**
Vessel 6	1.48	0.63	3.03	1.22	1.46	0.56	2.99	1.12	**0.52**	**0.19**	**1.22**	**0.41**
Vessel 7	1.56	0.60	2.43	0.98	1.55	0.58	2.40	0.91	**0.64**	**0.24**	**1.06**	**0.37**
Vessel 8	0.75	0.29	1.17	0.47	0.72	0.25	1.14	0.43	**0.34**	**0.11**	**0.63**	**0.19**
Vessel 9	0.75	0.29	1.48	0.55	0.72	0.25	1.46	0.51	**0.20**	**0.06**	**0.71**	**0.25**
Vessel 10	1.73	0.59	3.07	1.13	1.75	0.60	3.06	1.11	**0.81**	**0.28**	**1.13**	**0.37**
Vessel 11	1.93	0.65	3.05	1.09	1.94	0.66	3.03	1.05	**0.61**	**0.20**	**1.47**	**0.46**
Vessel 12	1.29	0.49	2.64	0.92	1.25	0.43	2.63	0.88	**0.52**	**0.18**	**1.19**	**0.37**
Vessel 13	1.92	0.67	2.63	0.95	1.90	0.64	2.61	0.93	**0.39**	**0.13**	**1.18**	**0.36**
Vessel 14	2.20	0.71	4.13	1.37	2.18	0.68	4.10	1.32	**0.92**	**0.32**	**1.50**	**0.45**
Vessel 15	2.95	1.01	4.72	1.54	2.94	0.94	4.69	1.47	**1.17**	**0.39**	**1.84**	**0.82**
Vessel 16	2.94	0.98	5.01	1.81	2.92	0.92	4.99	1.70	**1.23**	**0.38**	**2.41**	**0.83**

Note: L_2 norm - average distance. L_∞ norm - maximum distance.

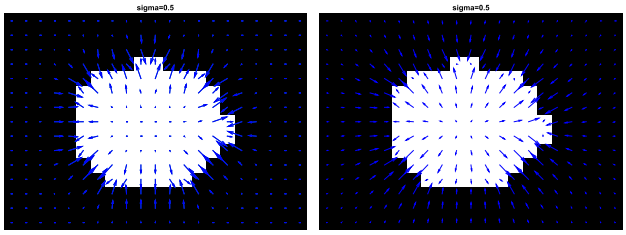

(a) (b)

FIGURE 6. A 2D example of gradient of edge map and GVF field. (a) Edge map, $\sigma = 0.5$. (b) GVF, $\sigma = 0.5$.

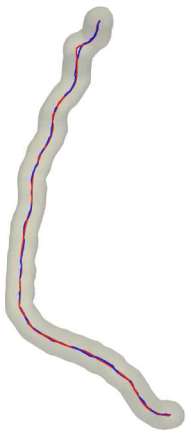

FIGURE 7. Ground truth centerline (*red*) and the computed centerline (*blue*) for Vessel 0.

the average distance and maximum distance in voxel space between the ground truth and computed centerlines were 0.61 ± 0.24 mm and 1.04 ± 0.38 mm, respectively. While for GVFFM method, the average distance and maximum distance in voxel space between the ground truth and computed centerlines were 0.25 ± 0.16 mm and 0.45 ± 0.21 mm, respectively.

Further quantitative validations were performed using the above 17 synthetic vessel models, according to three different overlap measures (overlap (OV), overlap until first error (OF) and overlap with the clinically relevant part of the vessel (OT)) [32], [33]. Table 3 compares the overlap measure evaluation results of the proposed GVFFM method with Van's method and DTFM method. The proposed GVFFM method is found to achieve higher OV, OF and OT measures for 16 synthetic vessel models among all the tested datasets. This is mainly because the new GVF based speed image avoids forming medial surface, which is capable of driving the discrete centerline tracking as close to real medial axis as possible. The average OV, OF and OT measures for Van's method are 93.3%, 85.2% and 93.0%, respectively. The average OV, OF and OT measures for previous DTFM method are 93.6%, 85.6% and 93.3%, respectively. While for the proposed GVFFM method, the three measures can be, respectively, up to 98.2%, 91.7% and 98.3%. The proposed method can therefore outperform the previous Van's and DTFM method. Meanwhile, the proposed GVFFM method is able to achieve OV measure of 100% for two vessel models, and OT measure of 100% for three vessel models. The only synthetic vessel model that the GVFFM method achieves lower overlap measures (OV, OF and OT) is Vessel 2. However, the reductions of all the three measures are marginal, which might be explained by the existence of high curvature areas and artifacts.

Furthermore, the proposed algorithm was performed on the testing set (24 datasets) of the Rotterdam coronary CTA database, and compared to another seven automatic centerline extraction method [14]. Table 4 shows the comparison with other automatic centerline extraction methods using the overlap metrics. The proposed method outperforms all the other automatic methods regarding OV and OT, and ranks second on OF.

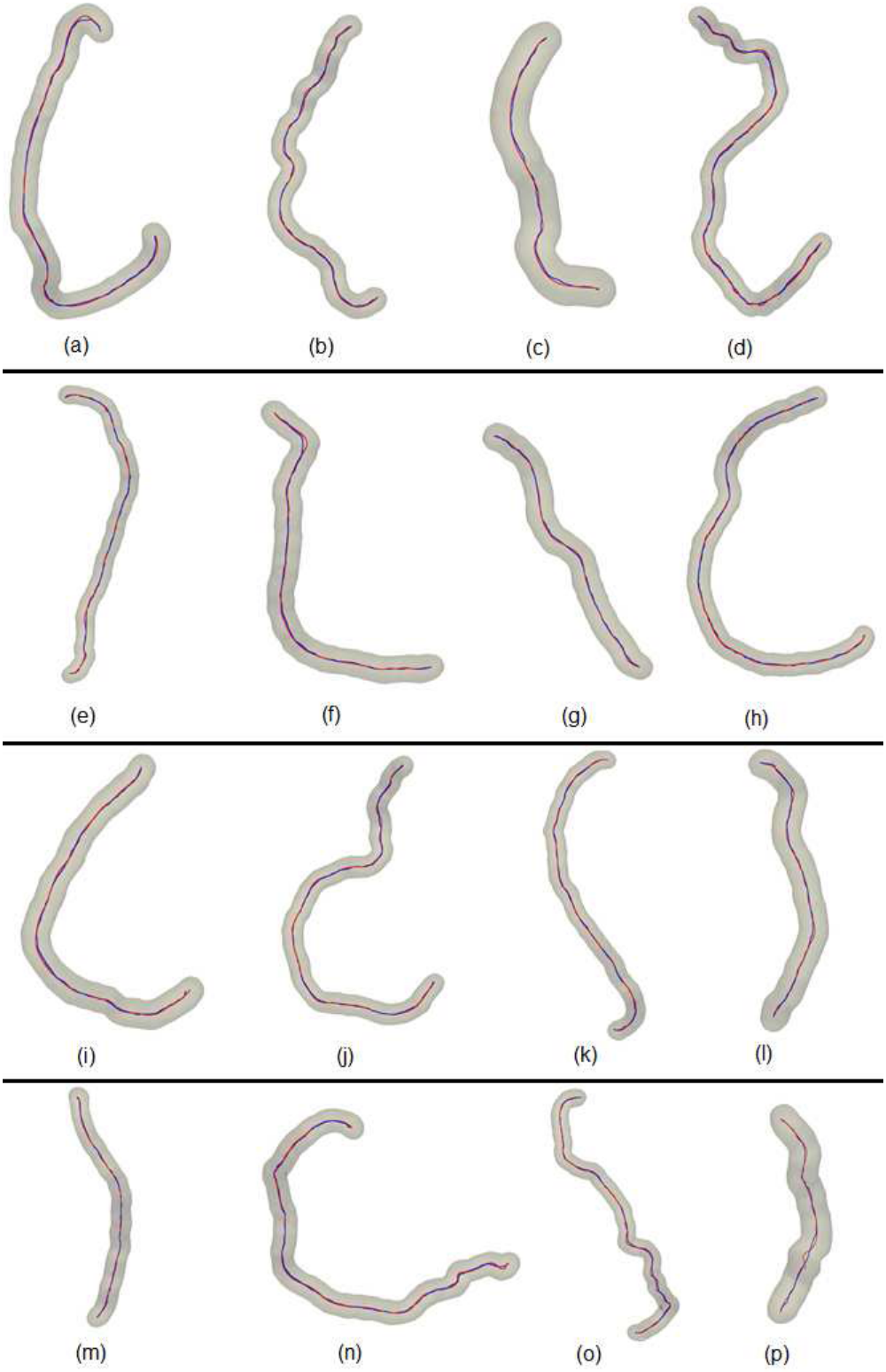

FIGURE 8. Computed centerline results (*blue*) and ground truth centerlines (*red*) for synthetic vessel models Vessel 1-16.

In addition, we tested the total running time of centerline extraction for all the three algorithms. Synthetic vessel model Vessel 0 was used as the reference model. The total processing time for each case includes two parts, distance map computation time and single branch tracking time. In Fig. 9 we compare the two-stage processing time for

TABLE 3. A comparison of computed three overlap measures between the obtained centerline and the ground truth centerline for Van's method, DTFM method and GVFFM method.

	Van's Method [15]						DTFM Method [16]						GVFFM Method					
	OV		OF		OT		OV		OF		OT		OV		OF		OT	
	%	Score	%	Score	%	Score	%	Score	%	Score	%	Score	%	Score	%	Score	%	Score
Vessel 0	93.8	52.7	90.0	42.4	94.3	45.6	94.4	53.1	90.2	42.5	94.5	45.8	**99.6**	**57.1**	**91.2**	**46.4**	**99.6**	**50.1**
Vessel 1	95.8	45.6	89.3	41.4	92.9	41.6	95.2	45.2	89.2	41.3	92.7	41.3	**98.5**	**50.1**	**94.1**	**48.5**	**98.5**	**49.4**
Vessel 2	92.7	46.5	72.0	40.4	92.7	46.6	**93.3**	**46.9**	**72.6**	**40.9**	**93.4**	**47.2**	93.2	46.8	70.5	35.6	93.3	47.0
Vessel 3	94.2	66.0	92.3	77.3	90.7	48.5	94.5	66.5	92.6	77.5	91.3	49.2	**99.7**	**85.5**	**99.5**	**90.3**	**98.6**	**89.9**
Vessel 4	94.3	55.9	93.1	66.8	93.1	47.8	95.1	56.3	93.7	67.5	93.6	48.1	**100.0**	**100**	**98.9**	**91.7**	**98.4**	**90.1**
Vessel 5	93.2	63.5	71.2	42.0	93.4	44.5	93.9	64.1	71.8	42.3	93.8	44.8	**98.8**	**93.3**	**76.8**	**46.4**	**98.7**	**49.5**
Vessel 6	93.5	67.1	73.6	45.8	93.4	48.0	93.8	67.3	74.5	46.1	93.7	48.2	**98.6**	**89.0**	**98.5**	**89.2**	**98.9**	**90.6**
Vessel 7	94.0	67.5	85.5	52.1	94.1	49.2	94.1	67.6	85.8	52.3	94.3	49.5	**98.9**	**91.4**	**99.7**	**91.6**	**100.0**	**100**
Vessel 8	95.1	69.2	90.8	58.0	94.1	50.2	95.7	69.4	91.3	58.4	94.9	50.7	**99.2**	**91.6**	**99.0**	**91.2**	**99.4**	**91.8**
Vessel 9	94.2	67.9	90.1	57.2	92.5	48.0	94.6	68.1	90.5	57.6	93.1	48.4	**98.7**	**91.4**	**98.5**	**91.0**	**99.2**	**91.5**
Vessel 10	93.6	44.3	93.5	43.8	95.0	49.9	93.5	44.2	93.1	43.6	94.7	49.5	**99.6**	**50.2**	**99.1**	**49.9**	**100.0**	**100**
Vessel 11	94.2	45.3	94.8	45.1	95.4	50.6	94.1	45.2	94.6	45.0	95.2	50.5	**98.6**	**91.3**	**98.9**	**91.2**	**98.3**	**91.1**
Vessel 12	94.1	46.2	94.4	45.3	94.3	49.8	94.6	46.3	94.8	45.7	95.1	50.4	**99.4**	**92.6**	**98.9**	**91.4**	**99.3**	**92.4**
Vessel 13	94.8	46.6	95.0	45.7	94.8	50.1	95.1	46.8	95.3	45.9	95.2	50.6	**100.0**	**100**	**99.7**	**92.7**	**99.8**	**92.9**
Vessel 14	92.9	43.7	92.7	43.2	94.1	48.9	93.0	43.8	92.9	43.4	94.3	49.1	**97.5**	**50.1**	**95.3**	**50.1**	**100.0**	**100**
Vessel 15	94.0	43.8	69.3	41.5	92.7	46.3	94.3	44.0	69.5	41.6	93.1	46.5	**98.4**	**50.2**	**73.9**	**76.2**	**98.6**	**50.3**
Vessel 16	82.3	40.2	62.9	35.1	82.1	40.2	82.7	40.7	63.2	35.4	82.4	40.6	**86.9**	**44.3**	**64.1**	**36.4**	**86.8**	**43.9**

Note: OV–Overlap, OF–Overlap until first error, OT–Overlap with clinically relevant part.

TABLE 4. Comparison with other automatic centerline extraction methods on the Rotterdam coronary CTA test set (24 datasets) using the overlap metrics.

Method	OV		OF		OT	
	%	Score	%	Score	%	Score
Proposed Method	**95.2**	**60.1**	75.7	54.3	**95.8**	**70.4**
Zheng's Method	93.5	53.4	**76.5**	**54.9**	95.6	70.0
GFVCoronaryExtractor	93.7	55.9	74.2	52.9	95.9	68.5
GVFTube'n'Linkage	92.7	52.3	71.9	51.4	95.3	67.0
SupervisedExtraction	90.6	53.8	70.9	49.0	92.5	61.2
DepthFirstModelFit	84.7	48.6	65.3	49.2	87.0	60.1
COR Analyzer	87.7	50.3	71.7	47.8	89.8	59.5
AutoCoronaryTree	84.7	46.5	59.5	36.1	86.2	50.3

both methods. For Van's method, the distance map computation time is 213.2 ± 31.8 seconds and the branch tracking time is 30.9 ± 3.6 seconds. For DTFM method, the distance map computation time is 215.4±32.5 seconds and the branch tracking time is 31.6 ± 3.7 seconds. On the other hand, the distance map computation time is 149.7 ± 13.6 seconds and the branch tracking time is 33.7 ± 3.2 seconds for GVFFM method. The new approach is able to improve the distance map computation efficiency by about 31%. At the same time, the branch tracking procedure costs almost the same time for all the three methods.

B. APPLICATION TO PATIENT STUDY

In this section, the presented coronary centerline computation framework was further applied over three different CTCA datasets in DICOM format (ccta 1, 14 and 22). In Table 5 we summarize the dataset size, resolution and computation time of both methods for each CTCA dataset. Before coronary artery segmentation, the vesselness diffusion was performed to the original CTCA datasets by applying the proposed diffusion filter. In this study, complete 3D segmentation results of

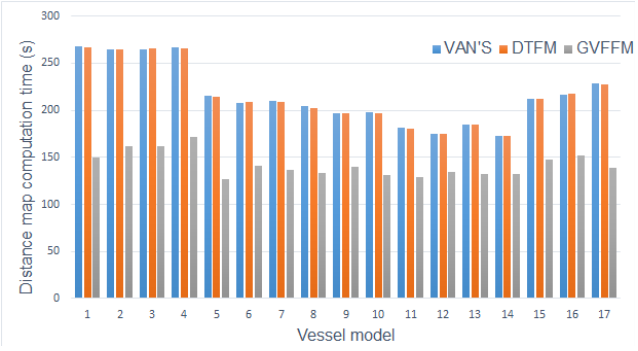

(a)

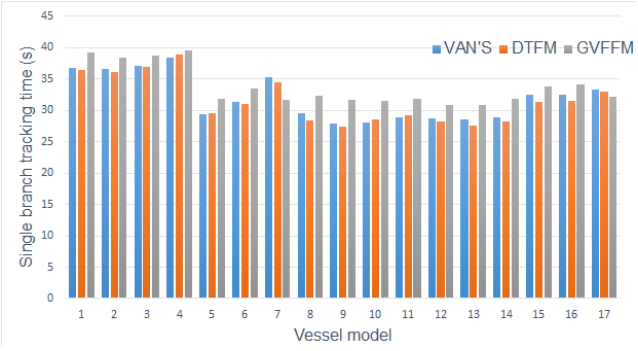

(b)

FIGURE 9. A comparison of processing time for the Van's, DTFM and GVFFM method. (a) Distance map computation time. (b) Single branch tracking time.

coronary artery trees were obtained from the CTCA datasets via Hessian filter and connected components based segmentation method [34]. In Fig. 10 we present the computed centerline results for three different CTCA datasets. The computed centerlines are continuous, naturally smooth and centrally located. In addition, no extra branches are generated

TABLE 5. Dataset size, resolution and computation time.

	Size	Resolution (mm^3)	Time (min)		
			Van's	DTFM	GVFFM
ccta 1	320×320×460	0.439×0.439×0.25	25	23	13
ccta 14	400×400×470	0.31×0.31×0.25	29	28	18
ccta 22	400×400×426	0.319×0.319×0.3	27	26	17

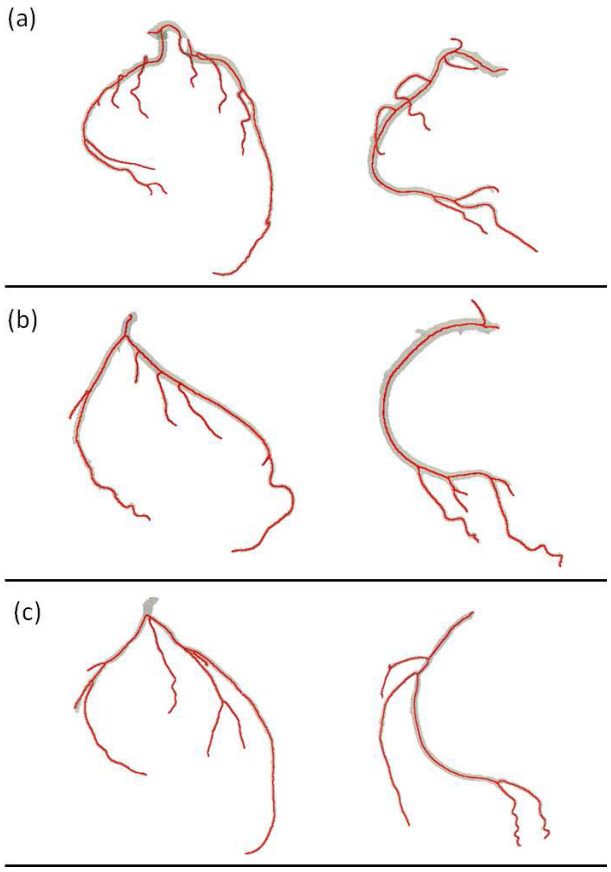

FIGURE 10. Computed centerlines (*red*) for LAD and left circumflex artery (LCX) (*left panel*), and right coronary artery (RCA) (*right panel*). (a) ccta 1. (b) ccta 14. (c) ccta 22.

by surrounding noises (Fig. 10(b)), because the centerline is tracked along the gradient descent in T and a termination criteria is introduced. The average processing time for each CTCA dataset is about 16 minutes, which provides a high efficiency for clinical practice.

The high accuracy benefits from the property of GVF field, which collapses to medial curve rather than medial surface, compared to conventional distance transformation based speed image. Moreover, the high order Runge-Kutta method and its numerical implementation in this work allows for accurate tracking of discrete centerline points. Thirdly, the proposed method possesses a good ability to handle the deviations. Therefore, the proposed method outperforms the DTFM method regarding the centerline accuracy, since the GVF field can collapse to the real central position of the tubular structure. On the other hand, DT based method may collapse to medial surfaces in stenosis positions (non-tubular), which may result in the deviation of the computed centerline from the ground truth centerline.

IV. DISCUSSIONS

In this work, an automatic and robust approach has been proposed for coronary artery segmentation and its centerline extraction to meet the needs of clinical practice. The presented method is capable of identifying each vessel centerline based on a wave front propagation technique to find its right way. For coronary artery segmentation, original Frangi's vesselness measure has some drawbacks, e.g., non-uniform staining. Moreover, Hessian analysis gives poor results on small branches of high curvature. We propose an enhanced Frangi's vesselness filter to steer main diffusion along the vessel and reduce background noises. As for the centerline extraction, each single branch is connected because the branch back tracking algorithm starts at the furthest geodesic point and terminates at the source points, which uses a constant step size. Meanwhile, newly detected points can intersect the previous centerline branch since the fast marching field is strong monotonic. Therefore, the entire centerline tree is connected, without any post-processing operation. Furthermore, the GVFFM method that we used can compensate for the problem of missing area or holes, which is capable of minimizing the possible deviation on the resulted centerline extraction.

In cardiovascular applications (e.g., IVUS), accurate stenosis identification plays an utmost role in the early diagnosis of heart diseases. Therefore, the centerline must possess the following features: centeredness, connectedness, topology preserving, uniqueness and robustness to noise [35]–[37]. Recall that the proposed centerline extraction framework computes the GVF field as the speed image, and drives a wave front propagation to compute the time arriving map, it can be proved to possess all the properties.

In the presented method, the GVF based speed image drives the centerline along ridges in the time-crossing map. We can change the value of γ and apply (20) on the CTCA image, to explore the effect of the field strength. The centerline strength is observed to be enhanced when decrementing the field strength γ. Finally, this approach is computationally efficient since a lower number of computations are needed (no distance map), and the branch tracking procedure is more efficient by using the proposed GVF based speed image.

V. CONCLUSIONS

In this study, we developed a fast and accurate framework for extracting coronary artery centerlines from real CTCA images. We have first proposed an enhanced Frangi's vesselness filter. The GVF field was then computed to develop a novel medial function of the 3D segmentation result. Finally, the centerlines were computed by using high order Runge-Kutta method, given the obtained time arriving map. Both the

accuracy and efficiency of the presented algorithm have been validated over 17 3D synthetic vessel models from real CTCA datasets. It showed that the proposed algorithm improved the overlap measure by 4.6% for OV, 6.1% for OF and 5.0% for OT. Besides, it was able to reduce the average error by 48%, and at the same time, reduce the average processing time by 26.1%. Furthermore, the new method was performed over several CTCA datasets from real patients. On average, it cost about 16 minutes for each dataset, compared with the time of 27.0 and 25.7 minutes per case in the previous work.

The experimental results demonstrated that the robustness and effectiveness have been improved for segmented coronary artery models and their centerlines tracking from cardiac CTA datasets. The new method is highly robust because the proposed centerline strength function does not form medial surfaces. Therefore, the back tracing procedure is guaranteed along the medial axis of the coronary arteries. Moreover, the new method is more efficient since it avoids calculating the distance field. Therefore, this algorithm should have more routine clinical applicability as a real-time coronary centerline computation tool.

ACKNOWLEDGMENT

The authors are very grateful to the National Heart Centre Singapore for the DICOM datasets.

REFERENCES

[1] J. R. Swedlow, I. Goldberg, E. Brauner, and P. K. Sorger, "Informatics and quantitative analysis in biological imaging," *Science*, vol. 300, no. 5616, pp. 100–102, 2003.

[2] S. K. Zhou, *Medical Image Recognition, Segmentation and Parsing: Machine Learning and Multiple Object Approaches*. New York, NY, USA: Academic, 2015.

[3] M. M. Fraz *et al.*, "Blood vessel segmentation methodologies in retinal images—A survey," *Comput. Methods Programs Biomed.*, vol. 108, no. 1, pp. 407–433, 2012.

[4] B. Bouraoui, C. Ronse, J. Baruthio, N. Passat, and P. Germain, "Fully automatic 3D segmentation of coronary arteries based on mathematical morphology," in *Proc. 5th IEEE Int. Symp. Biomed. Imag., Nano Macro*, 2008, pp. 1059–1062.

[5] H. Tek, M. A. Gülsün, S. Laguitton, L. Grady, D. Lesage, and G. Funka-Lea, "Automatic coronary tree modeling," *Insight J.*, pp. 1–8, Aug. 2008.

[6] C. Wang and O. Smedby, "An automatic seeding method for coronary artery segmentation and skeletonization in CTA," *Insight J.*, pp. 1–8, 2008.

[7] N. D. Cornea, D. Silver, and P. Min, "Curve-skeleton applications," in *Proc. IEEE Vis.*, Oct. 2005, pp. 95–102.

[8] S.-Y. Wan, E. L. Ritman, and W. E. Higgins, "Multi-generational analysis and visualization of the vascular tree in 3D micro-CT images," *Comput. Biol. Med.*, vol. 32, no. 2, pp. 55–71, 2002.

[9] S. Ukil and J. M. Reinhardt, "Smoothing lung segmentation surfaces in three-dimensional X-ray CT images using anatomic guidance," *Acad. Radiol.*, vol. 12, no. 12, pp. 1502–1511, 2005.

[10] E. Bullitt, S. Aylward, K. Smith, S. Mukherji, M. Jiroutek, and K. Müller, "Symbolic description of intracerebral vessels segmented from magnetic resonance angiograms and evaluation by comparison with X-ray angiograms," *Med. Image Anal.*, vol. 5, no. 2, pp. 157–169, 2001.

[11] S. R. Aylward and E. Bullitt, "Initialization, noise, singularities, and scale in height ridge traversal for tubular object centerline extraction," *IEEE Trans. Med. Imag.*, vol. 21, no. 2, pp. 61–75, Feb. 2002.

[12] L. Zhang *et al.*, "Automatic detection of three-dimensional vascular tree centerlines and bifurcations in high-resolution magnetic resonance angiography," *Invest. Radiol.*, vol. 40, no. 10, pp. 661–671, 2005.

[13] T. Wischgoll, J. S. Choy, E. Ritman, and G. S. Kassab, "Validation of image-based method for extraction of coronary morphometry," *Ann. Biomed. Eng.*, vol. 36, no. 3, pp. 356–368, 2008.

[14] Y. Zheng, H. Tek, and G. Funka-Lea, "Robust and accurate coronary artery centerline extraction in CTA by combining model-driven and data-driven approaches," in *Proc. Int. Conf. Med. Image Comput. Comput.-Assist. Intervent.* Berlin, Germany: Springer, 2013, pp. 74–81.

[15] R. Van Uitert and I. Bitter, "Subvoxel precise skeletons of volumetric data based on fast marching methods," *Med. Phys.* vol. 34, no. 2, pp. 627–638, 2007.

[16] H. Cui *et al.*, "Fast marching and Runge–Kutta based method for centreline extraction of right coronary artery in human patients," *Cardiovascular Eng. Technol.*, vol. 7, no. 2, pp. 159–169, 2016.

[17] Z. Li, Y. Zhang, G. Liu, H. Shao, W. Li, and X. Tang, "A robust coronary artery identification and centerline extraction method in angiographies," *Biomed. Signal Process. Control*, vol. 16, pp. 1–8, Feb. 2015.

[18] M. S. Hassouna and A. A. Farag, "Variational curve skeletons using gradient vector flow," *IEEE Trans. Pattern Anal. Mach. Intell.*, vol. 31, no. 12, pp. 2257–2274, Dec. 2009.

[19] H. Cui and Y. Xia, "Gradient vector flow field and fast marching based method for centerline computation of coronary arteries," in *Proc. Int. Conf. Intell. Sci. Big Data Eng.*, DaLian, China, Sep. 2017, pp. 597–607.

[20] P. H. Kitslaar, J. Dijkstra, B. Stoel, J. H. C. Reiber, M. Frenay, and E. Oost, "Connected component and morpholgy based extraction of arterial centerlines of the heart," *Midas J.*, pp. 1–8, Aug. 2008.

[21] A. F. Frangi, W. J. Niessen, K. L. Vincken, and M. A. Viergever, "Multiscale vessel enhancement filtering," in *Proc. Int. Conf. Med. Image Comput. Comput.-Assist. Intervent.*, 1998, pp. 130–137.

[22] R. Manniesing and W. Niessen, "Multiscale vessel enhancing diffusion in CT angiography noise ltering," in *Information Processing in Medical Imaging* (Lecture Notes in Computer Science), vol. 3565. Berlin, Germany: Springer, 2005, pp. 138–149.

[23] R. Manniesing, M. A. Viergever, and W. J. Niessen, "Vessel enhancing diffusion: A scale space representation of vessel structures," *Med. Image Anal.*, vol. 10, no. 6, pp. 815–825, 2006.

[24] A. K. Jain, *Fundamentals of Digital Image Processing*. Upper Saddle River, NJ, USA: Prentice-Hall, 1989.

[25] C. Xu and J. L. Prince, "Snakes, shapes, and gradient vector flow," *IEEE Trans. Image Process.*, vol. 7, no. 3, pp. 359–369, Mar. 1998.

[26] R. Courant, D. Hilbert, and F. C. Hoyt, "Methods of mathematical physics," *Phys. Today*, vol. 15, no. 11, pp. 62–63, 1962.

[27] S. Chang, D. N. Metaxas, and L. Axel, "Scan-conversion algorithm for ridge point detection on tubular objects," in *Medical Image Computing and Computer-Assisted Intervention* (Lecture Notes in Computer Science), vol. 2879. Berlin, Germany: Springer, 2003, pp. 158–165.

[28] S. Zhang and J. Zhou, "Centerline extraction for image segmentation using gradient and direction vector flow active contours," *J. Signal Inf. Process.*, vol. 4, no. 4, pp. 407–413, 2013.

[29] W. H. Press, B. P. Flannery, S. A. Teukolsky, and W. T. Vetterling, "Numerical recipes in C," *Contemporary Phys.*, vol. 10, no. 1, pp. 176–177, 1992.

[30] E. Suli, "An introduction to numerical analysis," *Math. Comput.*, vol. 30, no. 135, p. 664, 2003.

[31] C. Metz *et al.*, "3D segmentation in the clinic: A grand challenge II—Coronary artery tracking," in *Proc. Miccai Workshop 3D Segmentation Clinic: A Grand Challenge*, 2008, pp. 93–95.

[32] M. Schaap *et al.*, "Standardized evaluation methodology and reference database for evaluating coronary artery centerline extraction algorithms," *Med. Image Anal.*, vol. 13, no. 5, pp. 701–714, 2009.

[33] S. Ramcharitar *et al.*, "Integration of multislice computed tomography with magnetic navigation facilitates percutaneous coronary interventions without additional contrast agents," *J. Amer. College Cardiol.*, vol. 53, no. 9, p. 741, 2009.

[34] H. Cui *et al.*, "Coronary artery segmentation via hessian filter and curve-skeleton extraction," in *Proc. IEEE Conf. Biomed. Eng. Sci.* Dec. 2015, pp. 93–98.

[35] I. Bitter, A. E. Kaufman, and M. Sato, "Penalized-distance volumetric skeleton algorithm," *IEEE Trans. Vis. Comput. Graphics*, vol. 7, no. 3, pp. 195–206, Jul./Sep. 2001.

[36] Y. Zhou and A. W. Toga, "Efficient skeletonization of volumetric objects," *IEEE Trans. Vis. Comput. Graphics*, vol. 5, no. 3, pp. 196–209, Jul./Sep. 1999.

[37] Y. Ge, D. R. Stelts, J. Wang, and D. J. Vining, "Computing the centerline of a colon: A robust and efficient method based on 3D skeletons," *J. Comput. Assist. Tomogr.*, vol. 23, no. 5, pp. 786–794, 1999.

HENGFEI CUI received the B.S. and Ph.D. degrees in mathematical sciences from Nanyang Technological University, Singapore, in 2012 and 2017, respectively. In 2017, he joined the School of Computer Science and Engineering, Northwestern Polytechnical University, China, as a Post-Doctoral Fellow. His research interests include medical image processing, vessel segmentation, coronary centerline extraction, and computer-aided diagnosis for coronary stenosis.

His awards and honors include the Ministry of Education Scholarship, Singapore, and the Singapore Research Scholarship.

YONG XIA received the Ph.D. degree in computer science and technology from Northwestern Polytechnical University, Xi'an, China, in 2007. From 2007 to 2013, he was a Post-Doctoral Research Fellow with the School of Information Technologies, University of Sydney. He is currently a Professor with the School of Computer Science, Northwestern Polytechnical University. He has published over 40 journal papers, such as the IEEE-TIP, the IEEE-JBHI, *Information Fusion*, *Neurocomputing*, the IEEE-TBE, *Signal Processing*, CMPB, and the IEEE-TITB. His research interests include image processing, medical imaging, computer-aided diagnosis, multimedia computing, pattern recognition, and machine learning. He was the Awardee of the China 1000 Youth Talents Program.